Study on activity, stability limit and reaction mechanism of CO self-sustained combustion over the $LaMnO_3$, $La_{0.9}Ce_{0.1}MnO_3$ and $La_{0.9}Sr_{0.1}MnO_3$ perovskite catalysts using sugar agent

Junqin Huang[a,b], Zihao Teng[c], Running Kang[a,b], Feng Bin[a,b,d,*], Xiaolin Wei[a,b,d], Qinglan Hao[c], Kwun Nam Hui[e], Kwan San Hui[f], Baojuan Dou[c, *]

[a] *State Key Laboratory of High-Temperature Gas Dynamics, Institute of Mechanics, Chinese Academy of Sciences, Beijing 100190, PR China;*

[b] *School of Engineering Science, University of Chinese Academy of Sciences, Beijing 100049, PR China;*

[c] *Tianjin University of Science & Technology, Tianjin 300457, PR China;*

[d] *Dalian National Laboratory for Clean Energy, Dalian 116023, PR China;*

[e] *Institute of Applied Physics and Materials Engineering, University of Macau, Avenida da Universidade, Taipa, Macau, P.R. China;*

[f] *School of Engineering, Faculty of Science, University of East Anglia, Norwich Research Park, NR4 7TJ, United Kingdom.*

[*] ***Corresponding author. Tel.: +86 10 82544222; fax: +86 10 82544231***
E-mail address: binfeng@imech.ac.cn (F. Bin); bjdou@tust.edu.cn (B. Dou)

Abstract: The $LaMnO_3$, $La_{0.9}Ce_{0.1}MnO_3$ and $La_{0.9}Sr_{0.1}MnO_3$ catalysts are synthesized using sugar agent, and the CO self-sustained combustion is investigated, where the catalytic performance is decided by temperature with CO conversions of 10% (T_{10}), 50% (T_{50}), and 90% (T_{90}). The results show that self-sustaining combustion is successfully realized on the catalyst, and the order of activity decrease is as follows:

$La_{0.9}Ce_{0.1}MnO_3$ (with sugar)> $La_{0.9}Sr_{0.1}MnO_3$ (with sugar)> $LaMnO_3$ (with sugar)> $LaMnO_3$ (without sugar)> $La_{0.9}Sr_{0.1}MnO_3$ (without sugar)> $La_{0.9}Ce_{0.1}MnO_3$ (without sugar). Combined with the results of XPS, H_2-TPR, O_2-TPD and CO-TPD techniques, the excellent activity of $La_{0.9}Ce_{0.1}MnO_3$ (with sugar) can be attributed to the high content of Mn^{4+} ions and reactive oxygen vacancies enriched on the catalyst surface, sound low-temperature reduction, and uniform dispersion. Besides, in situ IR spectroscopy results indicate that the catalytic combustion of CO over manganese-based perovskite catalysts follows the L-H mechanism: the chemisorption of CO and O_2 takes place to produce monodentate carbonates and bicarbonate species, which then decompose to yield CO_2 release. The high-temperature stability test provides evidence that the $La_{0.9}Ce_{0.1}MnO_3$ (with sugar) gives 100% CO conversion and that the activities remain almost unchanged after reaction for 12 h, where the temperature of catalyst bed reaches about 717 °C. The results obtained are helpful to accept this technology on efficient and clean energy utilization in iron and steel industry.

Keywords: Self-sustained combustion; Perovskite; Carbon monoxide; Stability limit; Sugar agent

1. Introduction

The iron and steel industry has been widely accepted as the largest energy-consuming manufacturing industry worldwide and an essential source of greenhouse gas emissions. For about 70% of worldwide steel production, a basic

oxygen furnace (BOF) is employed to reduce impurities present in liquid metal, where the high-purity oxygen is blown by a supersonic jet into the metal bath to oxidize exceeded carbon in the molten iron, followed by multi-component off-gas up to 1600 ℃ from integrated steel mills. This tail gas embraces approximate 70% of carbon monoxide (CO) during steelmaking, corresponding to the heating value of almost 9 MJ/Nm^3. However, the concentration of CO varies with the steelmaking interval periodically and usually falls below 20% at the beginning and end of steel production. As the explosive nature of the CO and O_2 mixture, the tail gas produced during the steelmaking interval is first cooled by gasification cooling stack (Temperature range: 1600-700 ℃) coupled with water spray (Temperature range: 700-150 ℃) to remove the residual sensible heat, and then is released into the atmosphere through methane-combustion-sustaining flare burners.

Because of its intermittent and volatility, the released off-gas leads to the waste of instantaneous high-quality energy and excess CO_2 emissions (methane consumption), thus becoming an urgent technical problem about efficient and clean energy utilization need to be solved. Based on copper, cerium and zirconium mixed oxides ($CuCeZrO_x$), our previous studies discovered that the self-sustained combustion (via $CO \rightarrow CO_2$ self-exothermic reaction) could be employed to recover the chemical heat [1-3]. Such an identified scenario not only reduces the ignition temperature of the flameless combustion but also dilutes the explosion limit of CO/air mixtures to avoid the explosion. Since the mixed oxides are accessible to sinter at

high temperatures, however, the $CuCeZrO_x$ catalytic system is challenging to recover the sensible heat that should have been wasted during the water spray section.

Perovskite oxides, like $LaMnO_3$, etc., have been thoroughly studied as substitutes for catalytic oxidation in different fields. Relevant features include low cost, excellent adjustable element constitution, and thermo-stability (Calcination temperature > 900 ℃) [4]. The standard structure of perovskite oxides is ABO_3, where the A site consists of rare earth metals or alkaline-earth elements that are advantageous for stabilizing the composition, and the B-site cations are usually metal transition elements with multi-valence states that act as redox performance in the catalytic phase [5]. Except for the original form, cations at A and/or B sites can be replaced by foreign ones without disrupting the matrix structure, causing structural modifications associated with the production of oxygen vacancies and lattice defects, thereby meeting different reaction demands [6].

Alvarez-Galvan et al. [7] investigated the methyl ketone combustion on $LaBO_3$ (B= Co, Mn, Cr, Ni) perovskites. Among all the catalysts tested, the $LaMnO_3$ exhibited excellent activity, corresponding to the complete conversion at 297 ℃. According to Zhang et al. [8], the existence of oxygen species on the surface, that is, the oxygen which is easy to obtain and has enough fluidity, is the essential requirement for the high catalytic performance of $LaMnO_3$. With respect to the A-site substitution, a study of a train of $La_{1-x}Sr_xMnO_3$ perovskites ($0 < x < 0.5$) prepared for methane catalytic combustion has confirmed that the BET surface area of these

catalysts enhances with high Sr substitution, in which the $La_{0.8}Sr_{0.2}MnO_3$ exhibits the highest intrinsic activity [9]. Also, Giroir-Fendler et al. [10] systematically studied the effect of A-site substitution on the catalytic performance of $LaMnO_3$ for the oxidation of vinyl chloride, with the activity following the order: $La_{0.8}Ce_{0.2}MnO_3$ > $La_{0.8}Mg_{0.2}MnO_3$ > $LaMnO_3$ > $La_{0.8}Sr_{0.2}MnO_3$. Here, the Ce-doped perovskite is active due to its low-temperature reducibility. Although many reports have linked catalytic oxidation of gaseous pollutants using $LaMnO_3$-based catalysts, no statistical evidence of catalytic ignition to achieve self-sustained combustion has yet been presented.

In this study, we propose a series of $LaMnO_3$ perovskites substituted by Sr or Ce at A site for studying activity descriptors and understanding the CO oxidation process. The relationship between the catalytic and structural properties of these perovskite oxides is studied using XRD, XPS and H_2-TPR, etc. As a complicated process, the catalytic ignition of CO presents a transition from low reactivity steady-state (intrinsic reaction kinetics stage) to high reactivity steady-state (self-sustaining catalytic combustion stage) due to heat transfer limitation. The O_2-TPD, CO-TPD and in situ infrared spectroscopy experiments are employed here to deeply understand the catalytic reaction mechanism of CO during ignition since potential heat/mass transfer process has not been observed in the low-reactivity state but appeared obviously in the high-reactivity state. The results obtained provide an estimation to abate CO using perovskite oxides and help the iron and steel industry use self-sustaining catalytic combustion technology to achieve efficient and clean energy utilization.

2. Experimental

2.1. Preparations of catalysts

The $LaMnO_3$ catalyst is synthesized via the sol-gel method. The $La(NO_3)_3 \cdot 6H_2O$ and $Mn(NO_3)_2 \cdot 4H_2O$ are dissolved in the given amount ethylene glycol solution containing 0% and 2% sugar as pore-forming agent respectively and stirred at 80 ℃ for 2 h. Then 10 ml of methanol is applied to the solution individually and the solution is acutely stirred before the colloidal gel is formed. After being stored at room temperature for almost 36 h, the resulting gel is dried at 110 °C for 24 h to create a gelatinous solid, which is then put in a crucible and calcined at 900 °C in stagnant air for 6 h. The $LaMnO_3$ catalysts with 0% and 2% sugar (sucrose) are denoted as LMO-W and LMO-SW, respectively. The substituted $La_{0.9}Ce_{0.1}MnO_3$ and $La_{0.9}Sr_{0.1}MnO_3$ catalysts with 0% and 2% sugar are also prepared by the sol-gel method, denoted as LCMO-W, LSMO-W (0% sugar), LCMO-SW and LSMO-SW (2% sugar), respectively.

2.2. Characterization

Powder X-ray diffraction (XRD) tests are conducted on an XD-3-automatic diffractometer (PERSEE) fitted with Cu Kα nickel-filtered radiation. The range of spectrum acquisition is from 10 to 80°, with a scan rate of 8° per minute and a step of 0.02°. X-ray photoelectron spectroscopy (XPS) is performed on the Kratos Axis Ultra

DLD spectrometer. Monochromated Al Kα (λ=1486.6 eV) is selected as the radiation source, and the operating voltage is 15 kV. The binding energies are calibrated using the C 1s (284.8 eV) adventitious carbon peak. Hydrogen temperature-programmed reduction (H_2-TPR) experiments are carried out on the TP-5080B Auto multifunctional adsorption instrument equipped, which loads a thermal conductivity detector (TCD). Each sample (30 mg) is pretreated in pure He at 500 °C for 30 minutes. After cooling to 50 °C, H_2-TPR measurements are recorded in 5% H_2/He (50 ml/min) and heated to 1000 °C at a rate of 10 °C/min.

The temperature-programmed desorption of oxygen and carbon monoxide (O_2- and CO-TPD) is also carried out on the TP5080B instrument by 5% O_2/He and 5% CO/He mixtures, respectively. After the pre-treatment of each sample (30 mg) at 500 °C for 30 min, it was fully absorbed in a pure O_2 or CO atmosphere at 50 °C for 30 minutes and then exposed in He flow to remove physically adsorbed O_2 or CO until the baseline stabilization occurred. The sample is then heated at 10 °C/min until reaching 1000 °C. The consumption of H_2, O_2, and CO is calculated quantitatively by integrating the TPR and TPD curves. In situ infrared (IR) spectra are recorded on a Bruker Tensor 27 instrument, which equips a self-designed magnetically-driven transmission cell equipped with an MCT detector with a resolution of 4 cm^{-1} and capable of 32 scans. About 20 mg of fresh catalysts are pressed into a self-supporting wafer, immobilized in a quarts IR cell, and heated at 300 °C in the flow of N_2 for 1 h to eliminate any impurities. When the temperature is cooled from 300 °C under N_2

flow to ambient temperature, the IR spectroscopy is collected as a background for this catalyst. Subsequently, the catalyst is exposed to a stream of 25% CO/N_2 or 25% $CO+25\% O_2/N_2$ at 30 ml/min for 0.5 h until saturation is reached. Then the spectra are collected based on the desorption process under the N_2 stream or continuous flow reaction process from ambient temperature to 200 °C with a heating rate of 10 °C/min.

2.3. Catalytic activity measurement

The catalytic activity of perovskite oxides for CO oxidation is investigated in a 4 mm inner diameter microreactor. 200 mg of catalyst is pre-pressed into sheets and sieved into 20-40 mesh, and then filled in the reactor. The feed gas of CO/air is introduced into the reactor and is controlled by mass flow controllers measuring ±1% accuracy over the full range. The total flow rate of each test is maintained at 200 ml/min. The activity evaluation, including the lean-combustion limit, is performed under steady-state conditions while the temperature is heated from room temperature to 400°C at a rate of 5°C/min, then turned off the heat source to monitor the combustion running auto-thermally. Two K-type thermocouples with a thickness of 0.5mm are used here: the first one, inserted in the center of the catalyst bed, is continuously monitoring the temperature; the second one, located in front of the catalyst bed, is used control to the furnace temperature. The main criteria to judge the self-sustained combustion should be that the room temperature is lower than the wall temperature and keeps steady for 10 min, and the two-dimensional temperature distribution on the

reactor surface (the emissivity of the surface is 0.87) can be collected by the FLIR T640 infrared camera (full-scale measurement precision of ±2%). An online gas analyzer (Maihak) is used to monitor the effluent CO, O_2 and CO_2 (CO range is 0% - 30%, accuracy is ± 2% FS; O_2 range is 0-10% - 40%, accuracy is ± 3% FS; CO_2 range is 0-10%, accuracy is ± 3% FS).

3. Results and discussion

3.1. XRD and XPS analysis of catalysts

The XRD patterns for all the catalysts are shown in Fig. 1. According to the conventional diffraction powder file, the main diffraction peaks (2θ=23.1°, 32.6°, 40.3°, 46.7°, 58.4°, and 68.3°) of LMO utterly match the usual perovskite phase of LaMnO (PDF#50-0299) with no other impurity [11], which correspond to typical crystal planes of (110), (200), (202), (220), (024) and (224) respectively [12]. Small diffraction peaks centered at 27.7° observed in LCMO are assigned to the fluorite structure of CeO_2 (PDF#81-0792) [13], and such a separation phase arises from the high loading ratio of cerium during the catalyst preparations. Similarly, the faint diffraction peaks centered at 15.6°, 27.9° and 48.7° can be observed in LSMO, which are indexed as the hexagonal phase of $SrMnO_3$ (PDF#24-1213) [14, 15]. No significant change is found for the peak intensity and width of LMO-W, LMO-SW, LSMO-W, LSMO-SW, and LCMO-W. However, the LCMO-SW exhibits the weaker diffraction peak of the perovskite phase than others since the addition of sugar frustrates agglomeration and crystallization of active metals during the calcination,

thus allowing the creation of smaller crystalline oxides [16].

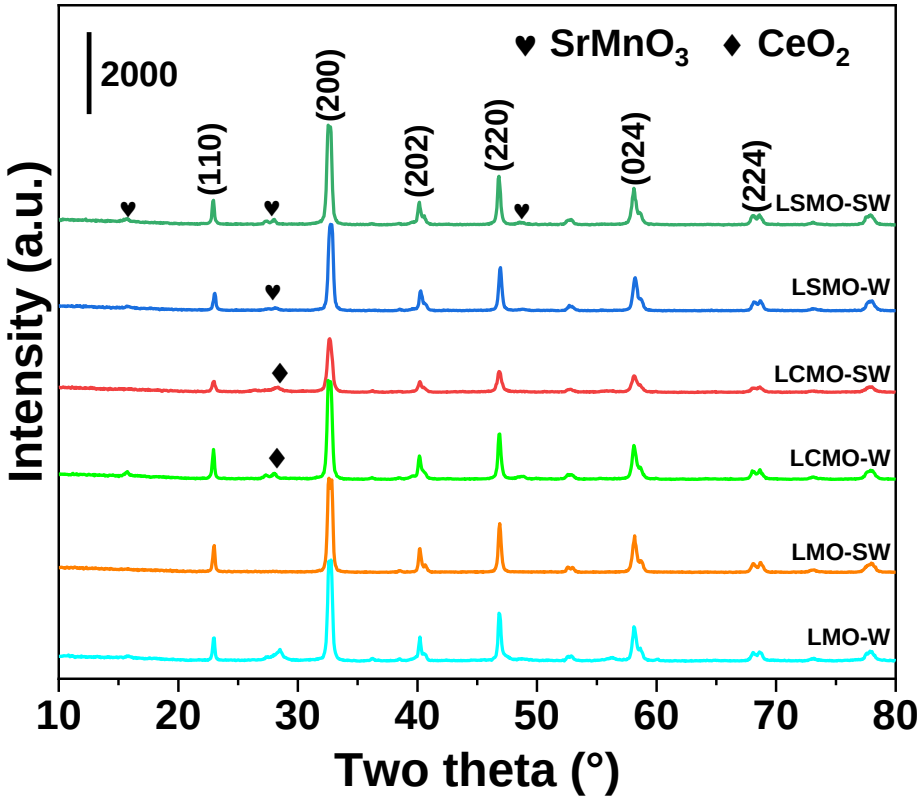

Fig. 1. XRD patterns of the catalysts.

XPS technique is used to analyze the chemical condition and the catalyst's surface structure. As illustrated in Fig. 2a, the La 3d core-level XP spectra of catalysts are typical of La^{3+} compounds [17]. The two peaks are separated into two lines $3d_{5/2}$ and $3d_{3/2}$ owing to a spin-orbit relationship, while each line is further separated by the shift of the electron from the oxygen ligands to the La 4f [18], corresponding to the peaks located at 834.4, 838.0, 851.2, and 854.8 eV, respectively. Two prominent peaks are observed in Fig. 2b, indicative of Mn $2p_{1/2}$, and Mn $2p_{3/2}$ for all catalysts. The asymmetrical Mn $2p_{3/2}$ peak at about 642 eV verifies the presence of at least two Mn valence states: 641.6 eV for Mn^{3+} and 643.5 eV for Mn^{4+}, respectively [19]. The O1s

spectrum in Fig. 2c exhibit two deconvoluted peaks: the first one at 529.3 eV can be related to the lattice oxygen (O_L) species, and the other one at higher binding energy (531.0 eV) can be correlated with the surface chemisorbed oxygen (Os) species [20].

The LSMO-W and LSMO-SW give Sr 3d spectra in Fig. 2d, which at 132.4 eV and 134.1 eV can be deconvoluted into two peaks. Such a phenomenon suggests that the Sr present in the +2 oxidation state only [21]. For the LCMO-W and LCMO-SW, the Ce 3d spectra (Fig. 2e) are decomposed into $3d_{5/2}$ and $3d_{3/2}$ spin-orbit pairs, represented by v and u, respectively. The four intense peaks v_0 (881.8 eV), u_0 (900.3 eV), v_3 (897.6 eV), u_3 (916.2 eV), and the two weaker peaks v_2 (888.0 eV) and u_2 (906.9 eV) can be assigned to different Ce 4f electron configuration in the final states of the Ce^{4+} species. The v_1 (883.1 eV) and u_1 (902.8 eV) peaks can be related to the final state of the Ce^{3+} species, which prefers the formation of vacancies of oxygen and unsaturated chemical bonds on the surface of the catalyst [22, 23]. The surface atomic ratios of the component La, Mn, Sr, O, Ce, and the contents of the surface species Mn^{4+}, O_L, and Ce^{3+} are generalized in Table 1, measured according to the relative peak areas of the XP spectra. It can be found that the catalysts synthesized with sugar increase the surface contents of Mn^{4+} and lattice oxygen because the $Mn^{4+}/(Mn^{4+}+Mn^{3+})$ and $O_L/(O_L+O_S)$ in the catalysts with sugar are higher than those without sugar. Considering the catalytic activity test described below, the surface Mn^{4+} cations on the surface are easily reduced to a low chemical state, which plays an essential role in the CO oxidation process. However, the Mn^{4+} cations with relatively

small amounts lead to the decrease of activity after the Sr addition into A sites of $LaMnO_3$, and hence more Mn^{4+} cations enriched on the catalyst surface are expected during catalyst preparation. Similar results can also be obtained via Huang et al. and Li et al. [24, 25]. Due to the presence of Ce^{3+} beneficial to forming vacancies, the LCMO synthesized with sugar obtains a higher ratio of Ce^{3+} species than that without sugar, facilitating oxygen mobility during CO oxidation.

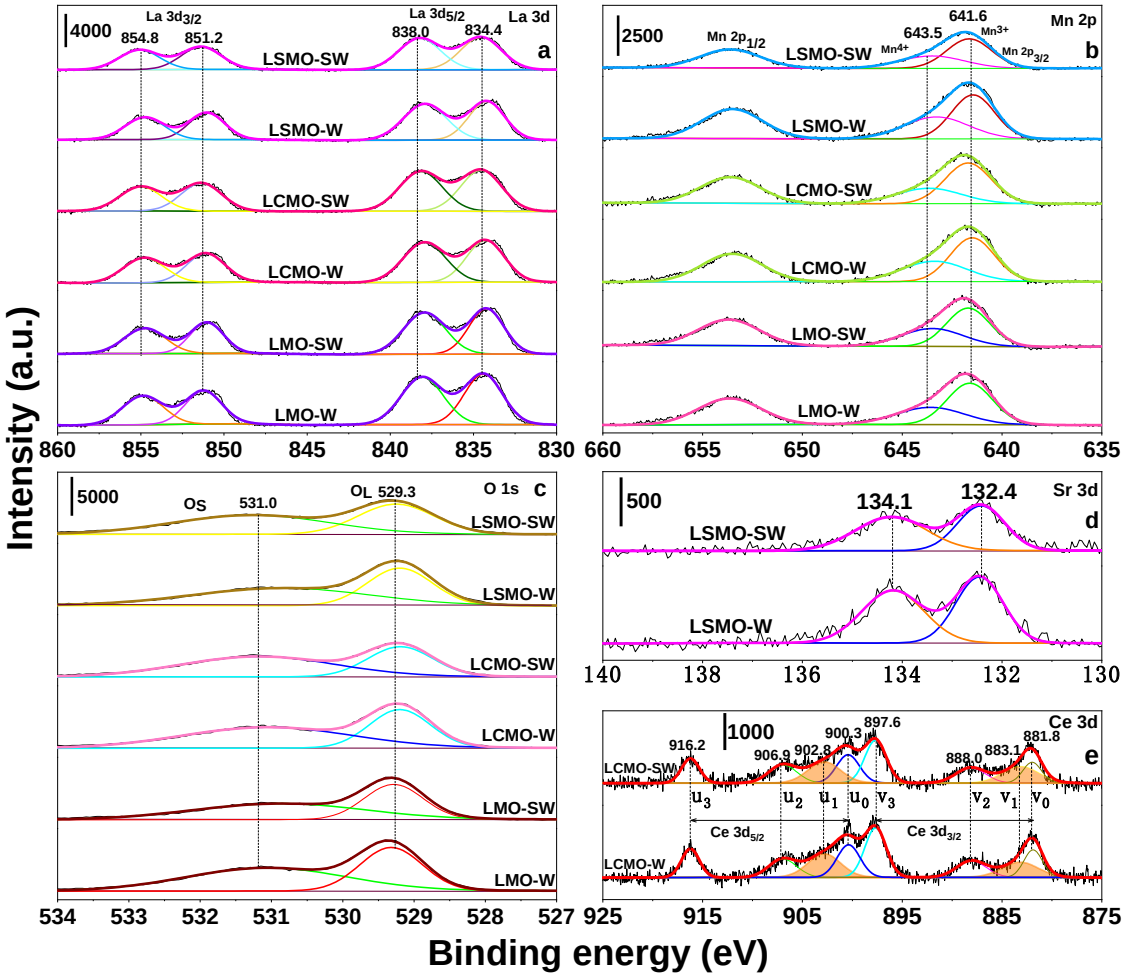

Fig. 2. XPS narrow spectra of La 3d (a), Mn 2p (b), O 1s (c), Sr 3d (d), and Ce 3d (e) over the catalysts.

Table 1 Surface compositions of catalysts derived from XPS analysis.

Catalyst	Surface element composition (at %)					$Mn^{4+}/(Mn^{4+}+Mn^{3+})$	$O_L/(O_L+O_S)$	$Ce^{3+}/(Ce^{3+}+Ce^{4+})$
	La	Mn	O	Sr	Ce			
LMO-W	17.3	14.5	68.2	/	/	40.1	42.2	/
LMO-SW	15.9	15.8	68.3	/	/	40.7	42.8	/
LSMO-W	17.1	12.7	67.5	2.7	/	34.9	38.3	/
LSMO-SW	14.7	14.2	68.3	2.8	/	40.7	39.9	/
LCMO-W	15.2	12.1	69.5	/	3.2	37.7	43.3	22.2
LCMO-SW	13.8	15.5	67.0	/	3.8	42.7	43.9	24.8

3.2. Temperature-programmed analysis of the catalysts

The H_2-TPR experiments investigate the reducibilities of the catalysts, with the profiles shown in Fig. 3. Two main reduction regions, for all the catalysts, are detected in the range of 200-600 and 600-850 °C. The low-temperature region (200-600 °C) can be separated into two separate sub-peaks: the β peak at about 398°C is attributed to the reduction of Mn^{4+} to Mn^{3+} [26-28]; the γ peak is allocated to the single-electron reduction of Mn^{3+} to Mn^{2+} in a coordination-unsaturated micro-environment at around 479 °C [29, 30]. In the other high-temperature region (600-850 °C), the δ peak with dominant intensity corresponds to the typical reduction of Mn^{3+} to Mn^{2+}. Such a phenomenon is similar to that reported by other group [15], where two reduction steps are observed for pure $LaMnO_3$, the first one in the temperature range 323–577 °C is attributed to the reduction of the fraction (35%) of Mn^{4+} to Mn^{3+}, and the other one

occurring during the isothermal step at 800 °C is due to complete reduction of Mn^{3+} to Mn^{2+}. Obviously, in the reduction process, the reduction of Mn^{2+} into Mn^{0} hardly occurred (200-850 °C) of the catalysts since the chemical state of Mn^{2+} is very stable in such a temperature range < 1000 °C [31]. H_2-TPR results also reveal that the Sr- and Ce-doped $LaMnO_3$ catalysts exhibit better reducibility than others in the overall high-temperature domain because the peak is decreased from 801 to 773 °C by 28 °C. By comparison, the β and γ peaks of the LCMO-W are abnormally located at 431 and 503 °C, respectively, which are abnormally higher than those of the other catalysts in the low-temperature area. The cerium addition into $LaMnO_3$ (LCMO-W) without sugar leads to crystallization into fluorite CeO_2 and perovskite crystals. With respect to the LCMO-SW, however, a new α peak appearing at 251 ° C may has partially been caused by the addition of sugar as a pore-forming agent, which promotes the formation of amorphous and relatively small oxide crystallites (determined by XRD analysis). More importantly, the existence of α peak is attributable to some cerium inserted into the lattice structure of $LaMnO_3$ to form solid solutions that include many Ce^{3+} ions (XPS analysis). The calculated amount H_2 consumption listed in Table 2 is within the range of 177.0-233.0 μmol/g for all the catalysts tested, where the H_2 uptakes of LMO-W and LMO-SW are 233.0 and 228.9 μmol/g that are higher than those of LSMO-W, LSMO-W, and LCMO-W. According to Kang et al. [32], the redox performance of the catalyst depends mainly on their reduction temperature rather than on hydrogen consumption. The LCMO-SW has a high H_2 consumption (α+β+γ=94.4

μmol/g) at the low-temperature region, together with the α peak appearing at 251 °C, and thus exhibits the highest excellent reducibility among all of the catalysts [10, 33].

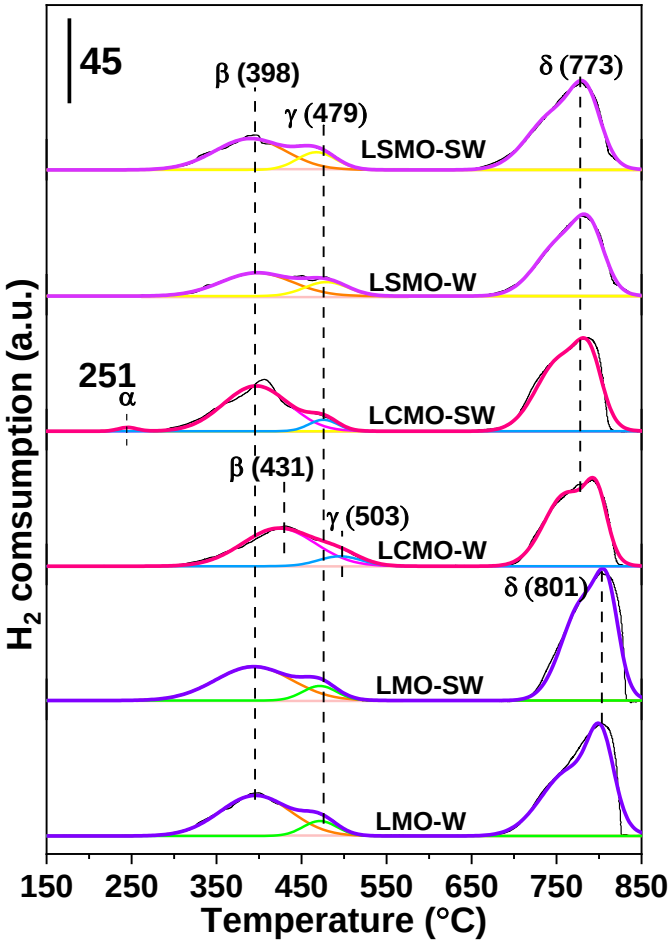

Fig. 3. H_2-TPR profiles of the catalysts.

Table 2 H_2 consumption (μmol/g) of catalysts derived from H_2-TPR analysis.

Catalyst	α	β	γ	δ	α+β+γ	Total
LMO-W	/	74.2	13.1	145.7	87.3	233.0
LMO-SW	/	66.7	12.7	149.5	79.4	228.9
LSMO-W	/	45.5	16.7	114.8	62.2	177.0
LSMO-SW	/	54.3	15.1	116.7	69.4	186.1
LCMO-W	/	69.1	10.7	112.2	79.8	192.0

LCMO-SW	2.0	83.1	9.3	135.6	94.4	230.0

The profiles of O_2-TPD that are seen in Fig. 4 show the two major regions of oxygen desorption. Region I, ranging from 200 to 550 °C, is assigned to the weakly adsorbed surface oxygen species [34]. The desorption of lattice oxygen species with different chemical environments is allocated to another area ranging from 550 to 900 °C [11]. In Region I, only LMO-SW and LCMO-SW catalysts exhibit the oxygen desorption peaks, revealing that the surface of these catalysts absorbed more oxygen, or the active oxygen can be readily released from the surface or the surface oxygen vacancy. It is well known that the density of chemically adsorbed oxygen on the surface is considered to be a factor affecting the oxidation ability of perovskite catalysts since the catalytic reduction of CO is promoted with the increasing number of chemically absorbed oxygen species in the catalyst surface. In Region II, a tiny peak around 645 °C for the LSMO catalysts and relatively large peaks for other catalysts are observed. Such a phenomenon reveals that the substitution of Sr is unfavorable to the desorption of lattice oxygen. Especially for LMO-W, two desorption peaks are monitored about at 656 and 830 °C, which may arise from the discontinuity desorption activity of lattice oxygen under the thermal environment [35]. The related oxygen desorption potential is further determined by quantitatively integrating the O_2-TPD curve to help compare the oxygen mobility of catalysts (Table 3). It can be found that LCMO-SW exhibits the highest desorption amounts of oxygen among all the catalysts, suggesting its admirable surface oxygen capacity and oxygen

mobility. The sugar, as a pore-forming agent, can be decomposed in the calcination process. At the same time, some oxygen atoms in the catalyst precursor would be employed so as to produce abundant oxygen vacancies during calcination process, which lead to oxygen desorbed in the low temperature region in O_2-TPD (Region I). On the contrary, the LSMO possesses a low oxygen desorption rate in all areas, and Sr substitution negatively affects oxygen capacity and migration activity, even though the sugar is involved in the synthesis process.

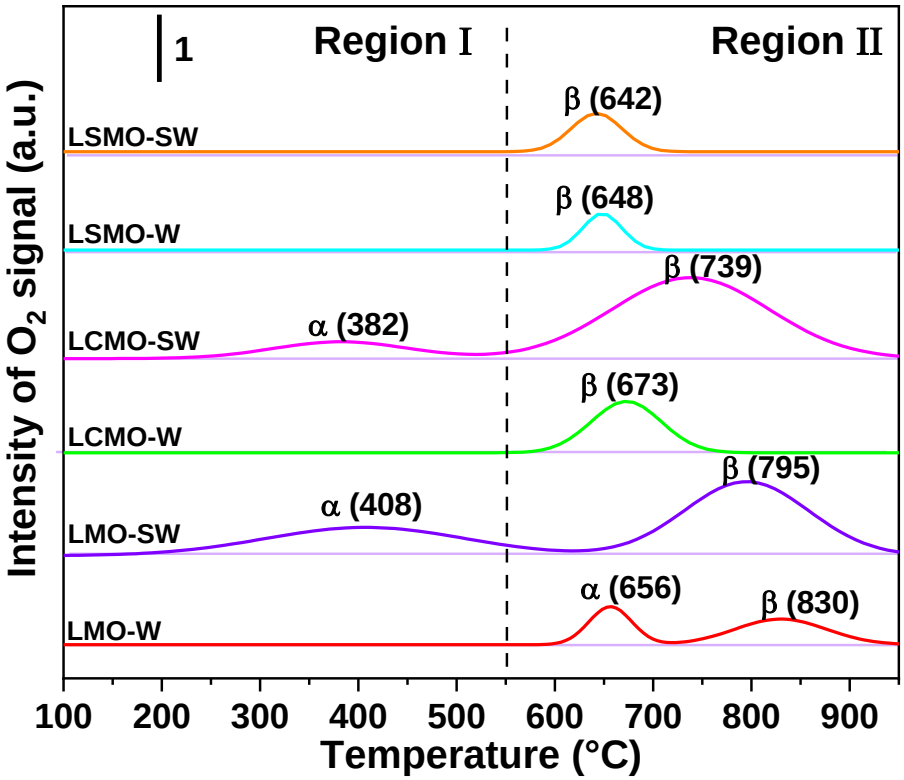

Fig. 4. O_2-TPD profiles of catalysts.

In the CO-TPD profiles (Fig. 5), a tiny desorption peak is observed in a range of 200–550 ℃ over the catalysts prepared with sugar, since the addition of sugar promotes to form amorphous perovskite crystal structure instead of crystallizing and agglomerating active metals during the calcination process. This makes it easier for

CO adsorbed on the catalytic surface to generate intermediate products such as carbonates and hydroxy carbonates etc., corresponding to the CO desorption (α peak) at low temperatures (419 °C for LMO-SW, 272 °C for LCMO-SW, and 492 °C for LSMO-SW, respectively) with low intensity [36]. Another desorption (β peak) at above 550℃ also presents for all the catalysts, related to the oxidation of bulk lattice oxygen [37]. Our previous studies confirmed that all the CO molecules adsorbed on the catalyst surface are desorbed in the form of CO_2 during the heating period, and no residual CO signal is observed, which shows that lattice oxygen indeed reacts with CO. The corresponding CO desorption capacity is calculated by integrating the CO-TPD curve quantitatively (Table 3). It can be found that LCMO-SW exhibits the highest desorption amounts of CO, indicating that the Ce substitution with a low level is beneficial to forming oxygen vacancies and improve oxygen mobility during CO oxidation.

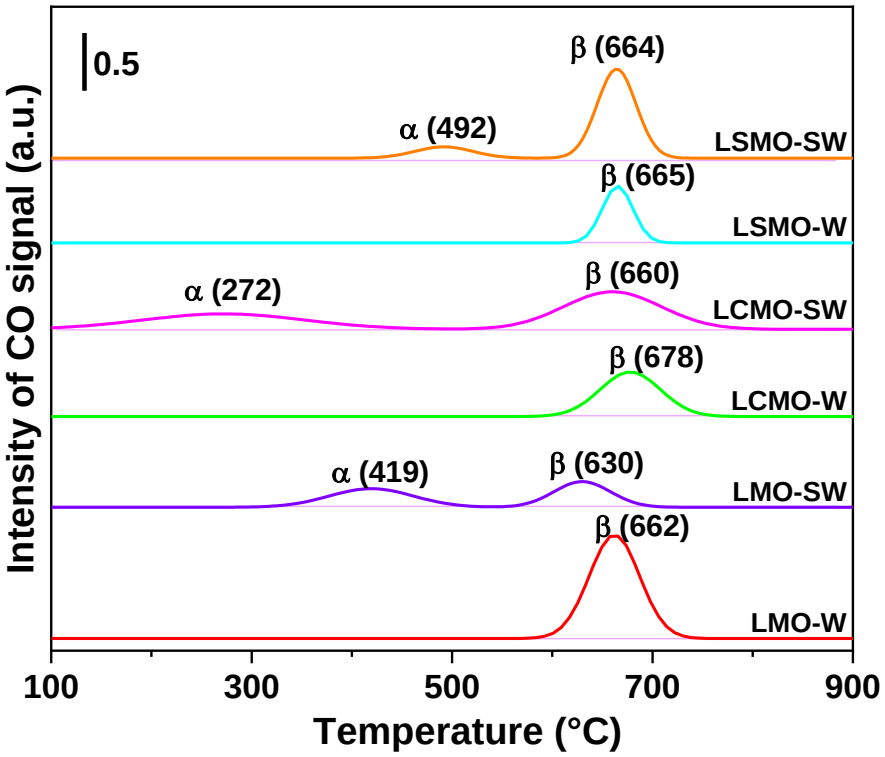

Fig. 5. CO-TPD profiles of catalysts.

Table 3 Amounts of O_2 and CO desorbed during the TPD experiments.

Catalysts	Uptake of O_2 (μmol/g)			Uptake of CO (μmol/g)		
	α	β	Total	α	β	Total
LMO-W	4	6	10	/	27	27
LMO-SW	15	20	35	8	7	15
LCMO-W	/	9	9	/	14	14
LCMO-SW	5	32	37	13	19	32
LSMO-W	/	4	4	/	9	9
LSMO-SW	/	5	5	3	8	11

3.3. Catalytic activity test

Figure 6 shows the change of CO conversion on the catalyst with reaction temperature. Under the reaction conditions (10% CO/air, total flow 200 ml/min), the CO conversion displays the sharp S-shape profiles during the heating process. All the catalysts tested suggest a light-off temperature of approximately 200 ℃, and under 400 °C, CO is wholly converted into CO_2. Take the LCMO-SW, for example, the first stage can be depicted as a slow induction process, starting at about 155 ℃ and then continuing at a relatively slow rate up to 183 ℃. The reaction is kinetically regulated here, revealed through the temperature of the catalytic bed near the controlled temperature. The second stage is the ignition process of the gas-solid interface. The temperature range is 183-210 ℃, and the rate of reaction is regulated via internal diffusion. The third stage concerns temperatures well beyond the ignition zone (> 210 ℃). Entering this step ensures that the reaction rate is regulated via external diffusion [38].

The parameters of T_{10}, $T_{50,}$ and T_{90} (i.e., reaction temperature at 10%, 50% and 90% CO conversion, respectively) are employed commonly to compare activities of the catalysts (Table 4), and the order of catalytic performance is followed by LCMO-SW> LSMO-SW> LMO-SW> LMO-W> LSMO-W> LCMO-W. It is evident that the catalytic combustor exhibits the typical highly exothermic reactions about CO oxidation with high CO feeding conditions. The rapid mass and heat transfer on the gas-solid interface facilitates CO self-sustained combustion at the CO conversion of 87.7%, 96.1%, 79% and 88.6% over the LCMO-SW, LSMO-SW, LMO-W and

LMO-SW, respectively, although the furnace temperature falls to room temperature (cooling process). By comparison, the CO self-sustaining catalytic combustion can not be maintained over the LSMO-W and LCMO-W since the reaction stopping gradually with the decrease of furnace temperature. The cooling lines of CO conversions move to lower temperatures than that of the heating lines, resulting in hysteresis. The formation of hysteresis may be due to the local exothermic effect of the oxidation reaction, so the reaction rate is not significantly affected even if the furnace temperature is lower than the ignition temperature. The stability of the LCMO-SW catalyst is evaluated under CO oxidation at the furnace temperature of 535 °C. As presented in Fig. 7, it is clear that the LCMO-SW gives 100% CO conversion and that the activities remain almost unchanged after reaction for 12 h. The temperature of the catalyst bed reaches about 717 °C in this case, considering the furnace temperature-controlled stably and the equilibrium of heat transfer during $CO \rightarrow CO_2$ self-exothermic reaction. This result indicates that the LCMO-SW is durable under high-temperature conditions.

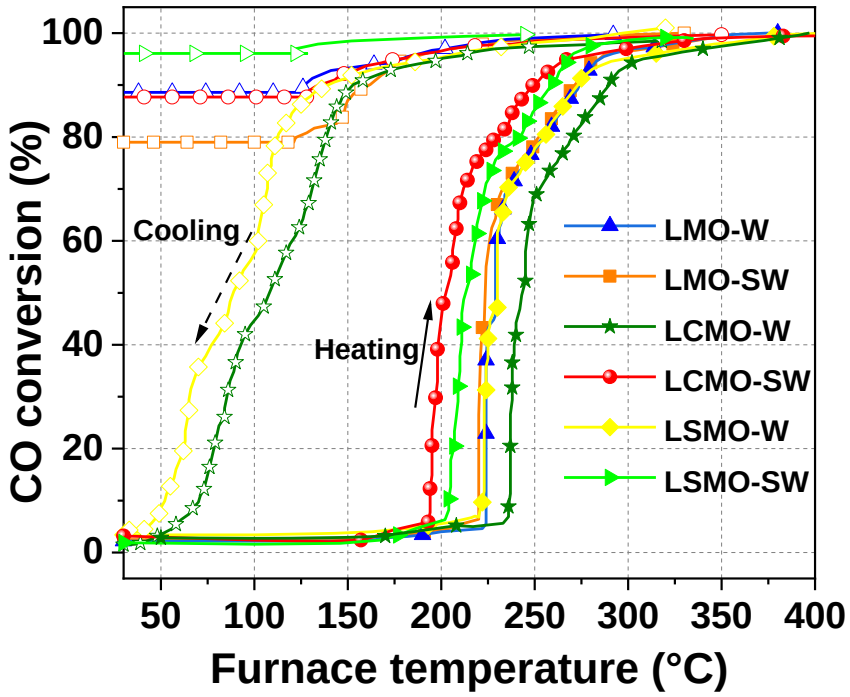

Fig. 6. CO conversion vs. furnace temperature for all of the catalysts.

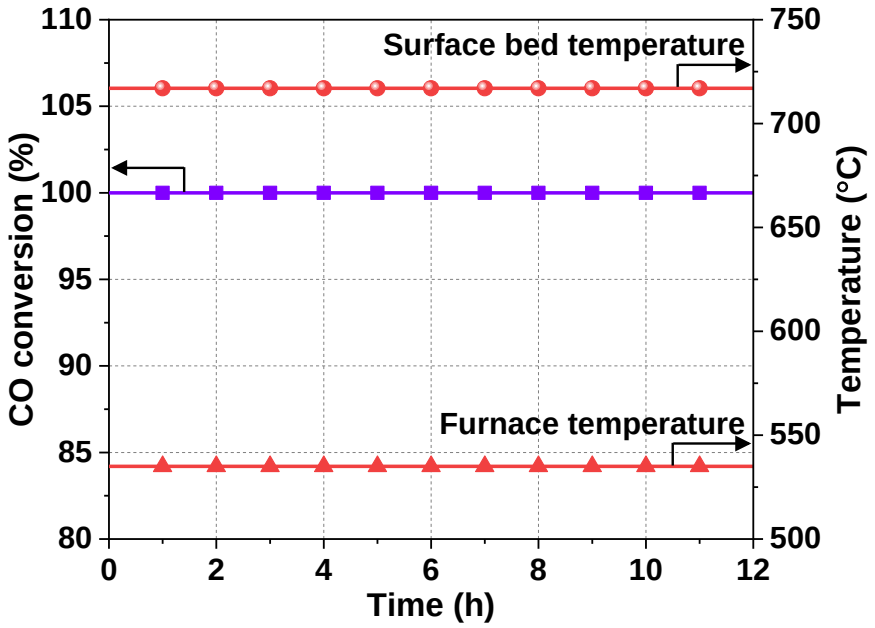

Fig. 7. Time-on-stream behavior of the LCMO-SW catalysts for CO oxidation at the furnace temperature of 535 °C (10% CO/air).

Table 4 Parameters of T_{10}, T_{50}, and T_{90} of the catalysts.

Catalyst	T_{10} (°C)	T_{50} (°C)	T_{90} (°C)

LMO-W	220	224	271
LMO-SW	224	229	273
LSMO-W	222	230	273
LSMO-SW	205	216	258
LCMO-W	237	245	289
LCMO-SW	195	205	248

3.4. Stability limit of CO self-sustained catalytic combustion

It is significant to determine the lean-combustion limits for the CO self-sustained combustion, considering the CO concentration periodically varies during the steelmaking process. Three catalysts, LMO-SW, LCMO-SW and LSMO-SW with relatively high activity, are put into the micro-reactor and the equivalence ratio of the fuel/air mixture is changed while maintaining the total flow rate invariable to determine the critical equivalence ratio ϕ_C via the Binary search. Taking the ϕ=1, ϕ=0 as the initial upper and lower bounds, the median value is taken for each experiment until it reaches the upper limit of the accuracy of the control valve, and then the equivalence ratio is determined as the critical equivalence ratio ϕ_C. As shown in Fig. 8a, the critical equivalence ratio over LCMO-SW, LMO-SW, and LSMO-SW are 0.212, 0.216, and 0.196, respectively. At the same flow rate, the lowest critical equivalence ratio of LCMO-SW means that it exhibits the highest activity among the catalysts evaluated because the catalytic combustion of CO leads firstly to form local

hot spots on the catalyst surface and thus, the catalyst with high performance only needs a lower stoichiometric ratio to provide a suitable local temperature for CO ignition. Furthermore, the 2D temperature fields in the reactor (Fig. 8a) also shows that the local hot spot for LSMO-SW is about 140 ℃, which is lower than that of the other two catalysts, namely 148 and 157.9 ℃ for the LMO-SW and LSMO-SW, respectively.

The same approach is taken to determine the critical equivalence ratio (ϕ_C) of catalyst LCMO-SW at different flow rates, with the results shown in Fig. 8b. With the increase of flow rate, the critical equivalence ratios (ϕ_C) are 0.303, 0.272, 0.182, 0.213 and 0.213, respectively. In other words, the critical equivalence ratios (ϕ_C) decrease first and then increase with increasing the flow rates, obtaining the minimum near 180 ml/min. The reason may be that the flow rate is too poor to realize the self-sustaining combustion of CO with small critical equivalence ratios. When the flow rate of gas is high, however, the input heat is increased so that the critical equivalent ratio is decreased. Further increasing the flow rate would increase the flow velocity, which takes away additional heat and results in more heat loss. In this case, the surface bed temperature (violet line in Fig. 8b) always rises with the flow rate to compensate for the heat loss.

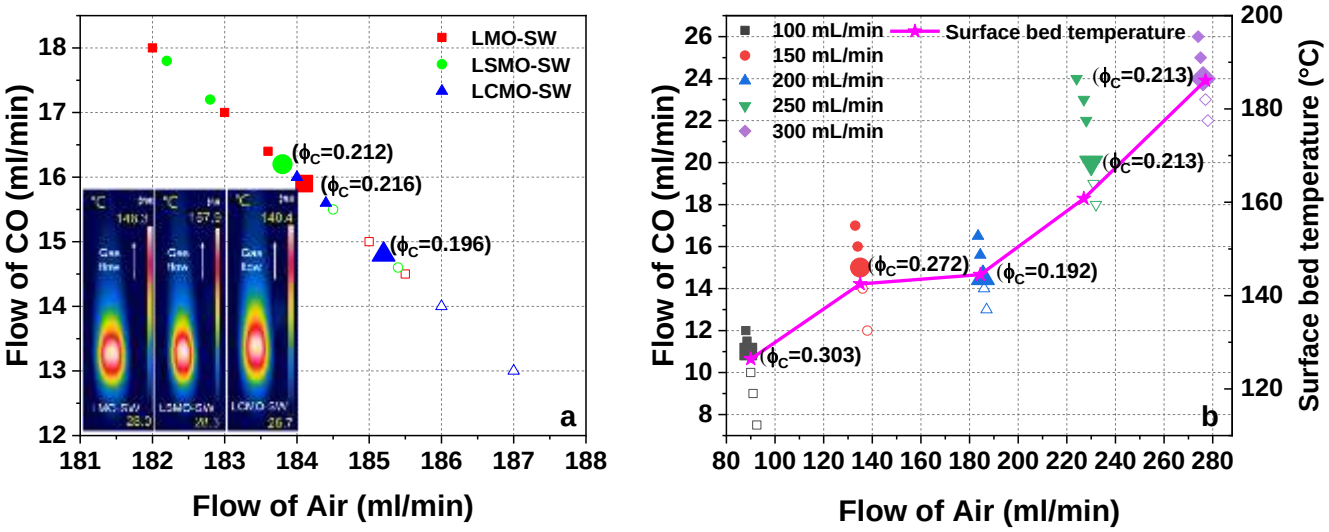

Fig. 8. Lean-combustion limits of CO self-sustained combustion over LMO-SW, LSMO-SW, and LCMO-SW catalysts (a) and over LCMO-SW catalyst in different flow (b).

3.5. In situ infrared spectroscopy analysis

Measurements of in situ IR spectra are performed to clarify the CO oxidation reaction process over the perovskite catalysts. The LCMO-SW, with the highest activity among all the catalysts tested, is first treated with 25% CO+25% O_2/N_2 (30 ml/min) at 25 ℃ for 0.5 h until the saturation is reached. After purging with pure N_2, the IR spectra are recorded in succession at 2 min intervals, shown in Fig. 9 (a). Table 5 presents the typical assignment of standard absorption bands. The spectrum, obtained at equilibrium for adsorption/desorption (0 min), only displays intense bands at 2175 and 2126 cm^{-1} [39], which can be assigned to gaseous CO signals. When

purging with pure N_2, the intensity of gaseous CO decreases monotonously with time and disappears entirely at 10 min, without any intermediate species such as carbonyls (2000-2200 cm^{-1}) and carbonates (1200-1800 cm^{-1}) left. The LSMO-SW catalyst is treated by the same method, and the infrared image similar to that of LCMO-SW catalyst is obtained, as shown in Fig 9 (b).

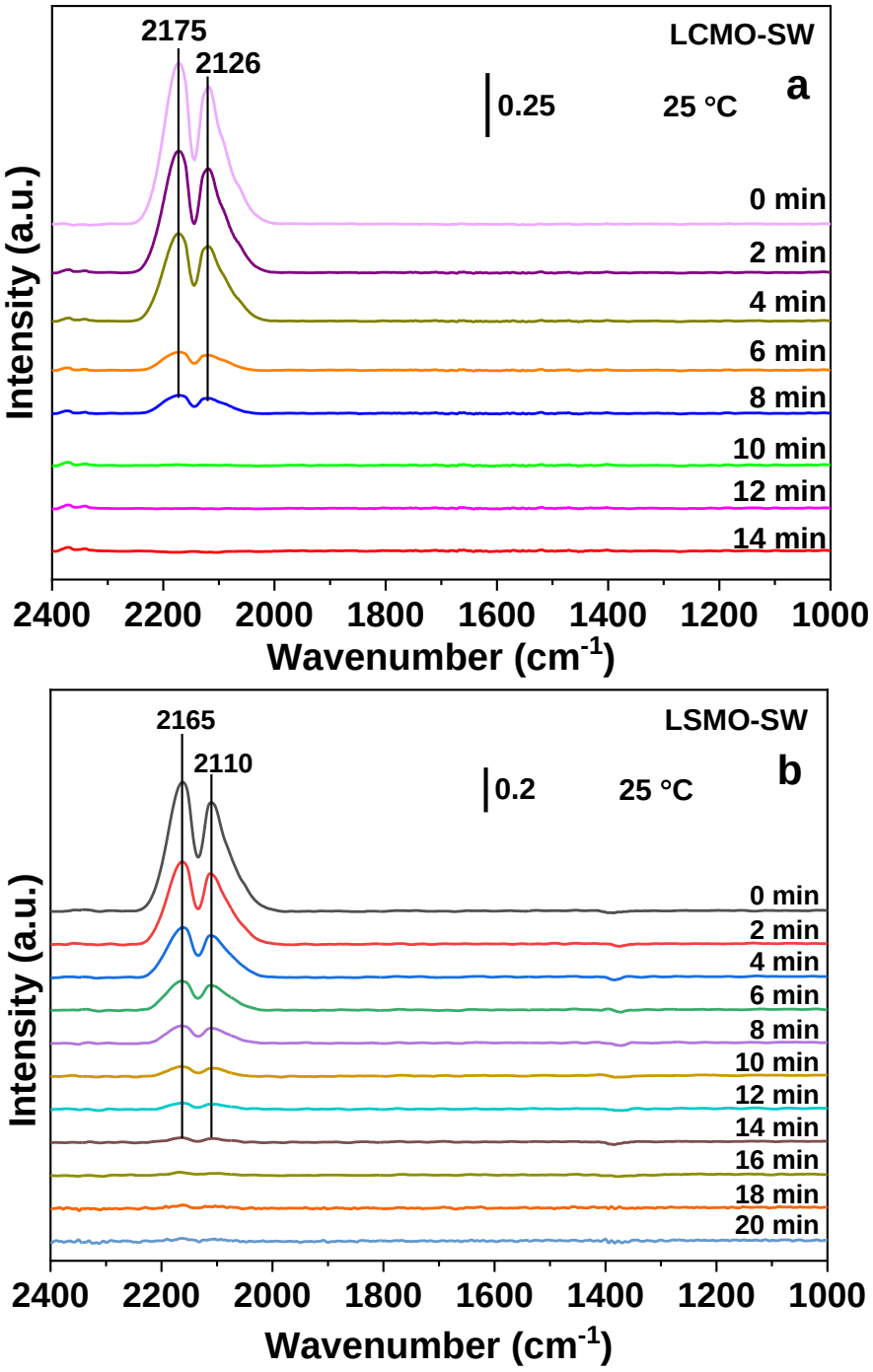

Fig. 9. IR spectra of the LCMO-SW catalyst (a) and LSMO-SW catalyst (b) arising from 25% CO+25% O_2/N_2 adsorption/desorption are recorded by 2 min interval under the ambient temperature condition.

Table 5 Typical vibrational wave numbers of different adsorbed species

Species	Adsorption bands (cm^{-1})	Ref.
CO	2110-2175;	[39]
bicarbonate	1632	[40]
monodentate carbonates	1398-1501	[41]
CO_2	2380-2300	[42]

IR spectra of the LCMO-SW catalyst under 25% CO/N_2 continuous stream are shown in Fig. 10a. When the temperature rises from room temperature to 170 ℃, there are only two intense peaks at 2175 and 2126 cm^{-1} corresponding to the gas CO signals. Interestingly, three new peaks (1632, 1501 and 1398 cm^{-1}) derived from the coordinated CO_x with the diminished cations are growing at the temperature ≥180 ℃, where the peak located at 1632 cm^{-1} comes from superficial bicarbonate species [40], and the peaks at 1501 and 1398 cm^{-1} are attributable to the monodentate carbonates [41], respectively. Simultaneously, the peak of gaseous CO reduces obviously between 180 and 200 ℃, but the peak of CO_2 bands at 2366 and 2336 cm^{-1} increased instead [42], confirming to achieve CO oxidation. When 25% CO+25% O_2/N_2 continuous stream has been introduced into the reactor (Fig. 10b), the intensity of the surface carbonates, bicarbonates and gaseous CO_2 signals are more substantial, but their corresponding beginning temperature (150 ℃) are lower than those under 25%

CO/N_2 continuous stream, demonstrating that CO can be easily oxidized over the LCMO-SW catalyst in the presence of O_2. The infrared curve of LSMO-SW is also shown in Fig. 11. It can be seen that the peak type change of LSMO-SW is similar to that of LCMO-SW, but the activity is poor. This may be the result of Sr inhibiting more Mn^{4+} ions. It can be inferred that the reaction pathways of LSMO-SW and LCMO-SW are similar according to their infrared diagrams.

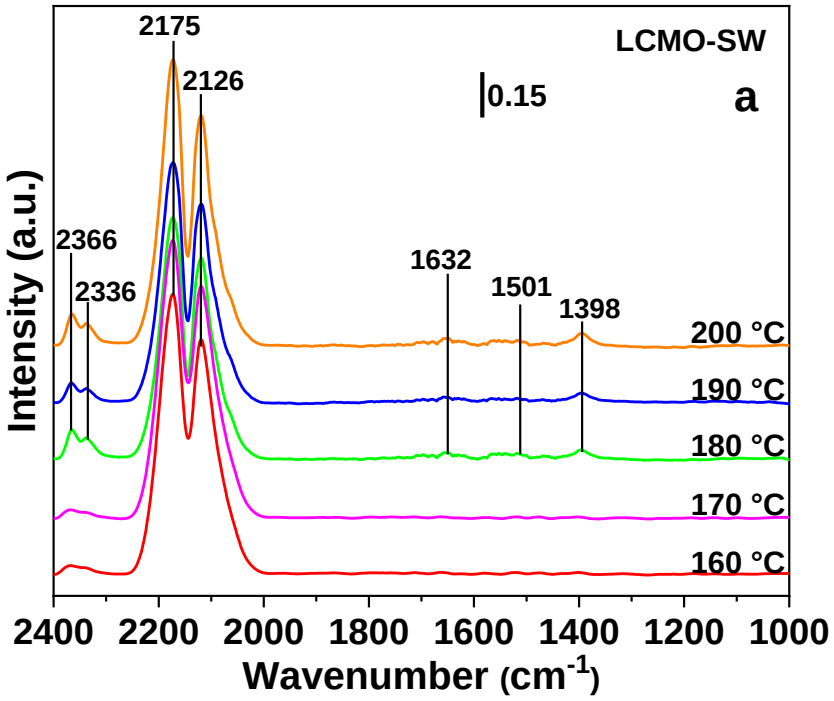

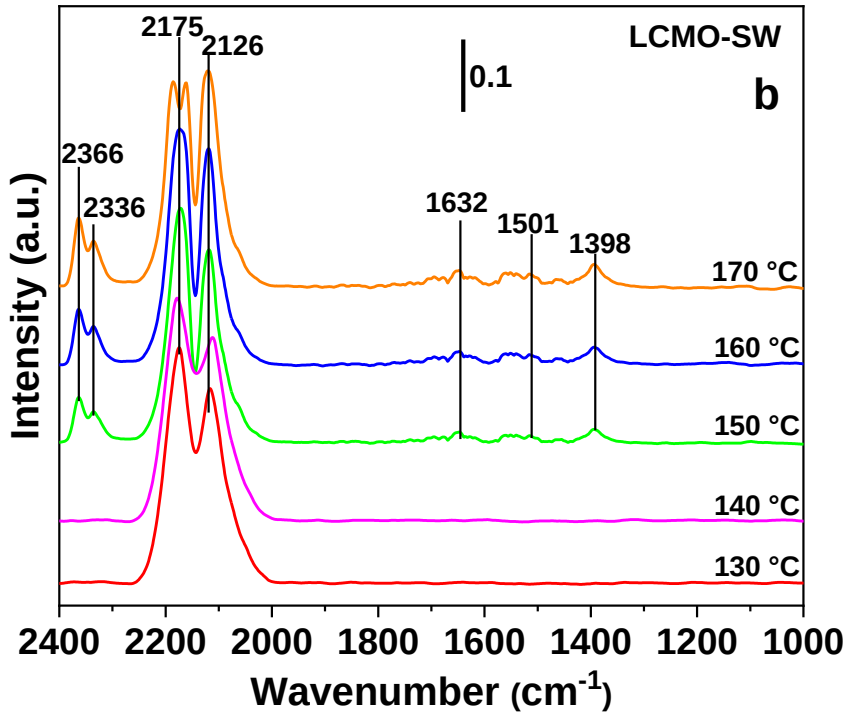

Fig. 10. IR spectra of LCMO-SW catalyst for the CO oxidation at 10 ℃ intervals under 25% CO/N_2 (a) and 25% $CO+25\% O_2/N_2$ (b) continuous stream conditions.

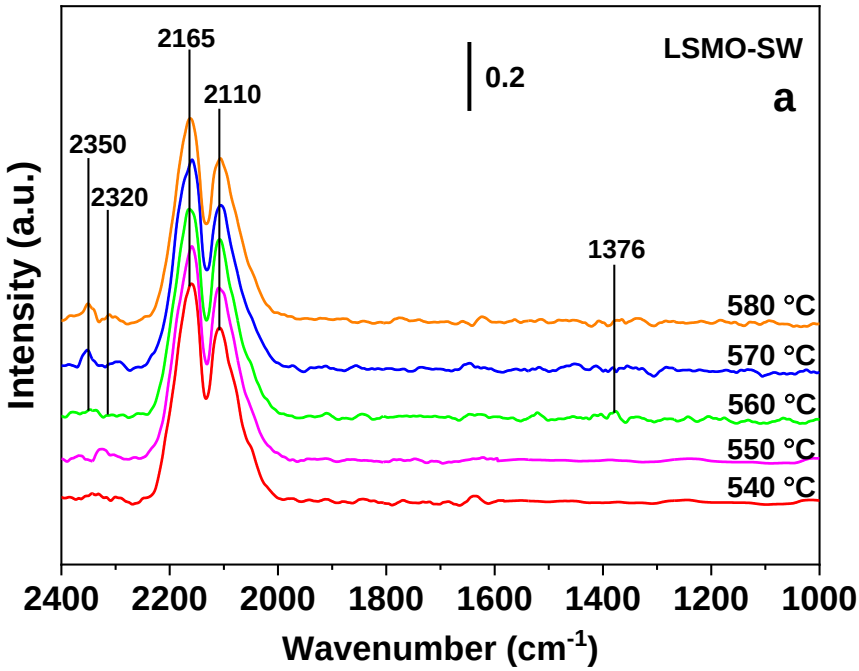

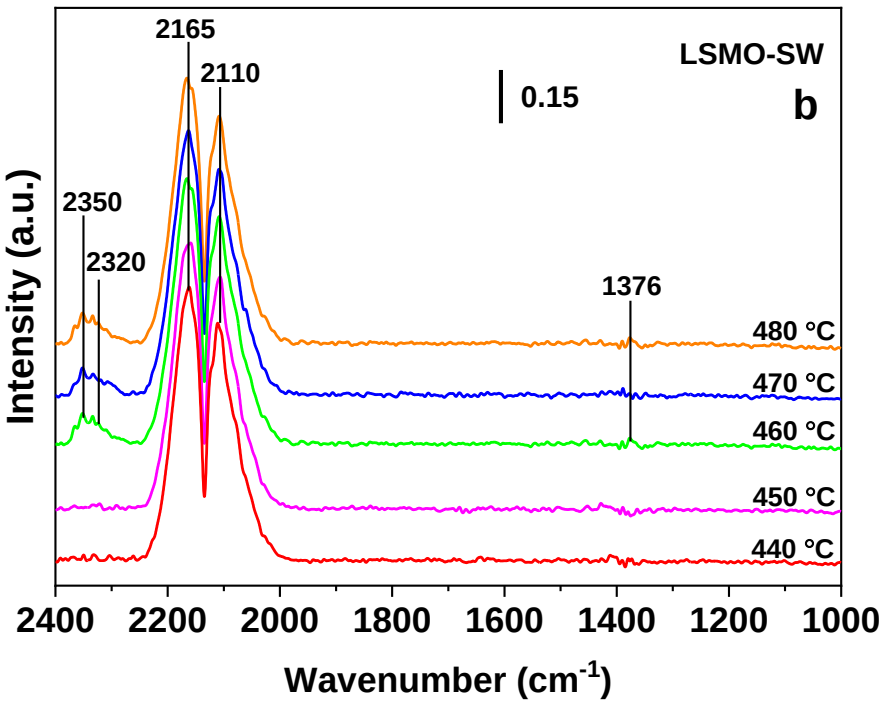

Fig. 11. IR spectra of LSMO-SW catalyst for the CO oxidation at 10 ℃ intervals under 25% CO/N_2 (a) and 25% CO+25% O_2/N_2 (b) continuous stream conditions.

Based on the above results, it can be inferred that the catalytic combustion of CO over the manganese-based perovskite catalysts follows the Langmuir-Hinshelwood (L-H) mechanism [43], and the proposed reaction pathway is exhibited in Fig. 12. The L-H mechanism involves that CO is adsorbed on oxygen atom linked to manganese and O_2 on oxygen vacancies over the LCMO-SW catalyst, thus forming monodentate carbonates and bicarbonate species, which then decompose to yield CO_2 release with increasing temperature. The results of IR spectra provide evidence that the peaks associated with monodentate carbonates and bicarbonates increase with increasing temperature (Fig. 10). The explanation may be that rising temperatures results in a growing amount of manganese ions with a high valence state (+4) reduced to a low valence state (+3) to adsorb CO [44]. According to the XPS analysis, the Ce

introduction into A sites of $LaMnO_3$ (LCMO-W) increases the surface content of Mn^{4+}, relative to that of LMO-W and, on the opposite, the Sr introduction into A sites (LCMO-W) inhibits the formation of Mn^{4+}. The high Mn^{4+} ratio raises the average oxidation state of manganese so as to form crystal defects [45]. Also, as a pore-forming agent, the catalysts synthesized with sugar not only leads to exposing more Mn^{4+} than that synthesized without sugar, but also hinders the agglomeration of active metal particles. As a result, part of perovskites as amorphous form promotes the low-temperature reducibility (H_2-TPR and CO-TPR). The LCMO-SW exhibits the highest catalytic performance among all the catalysts tested, which may have been partially caused by the Mn^{4+} cations with the highest level. The relatively high activity is probably also attributable to the presence of Ce^{3+} in the LCMO-SW. As a pore-forming agent, the sugar is decomposed in the calcination process, and some oxygen atoms in catalyst precursor are employed to produce Ce^{3+} ions or abundant oxygen vacancies. Hence the oxygen vacancies and unsaturated chemical bonds produced on the catalyst surface facilitates the oxygen mobility (O_2-TPD) during CO oxidation [46-48].

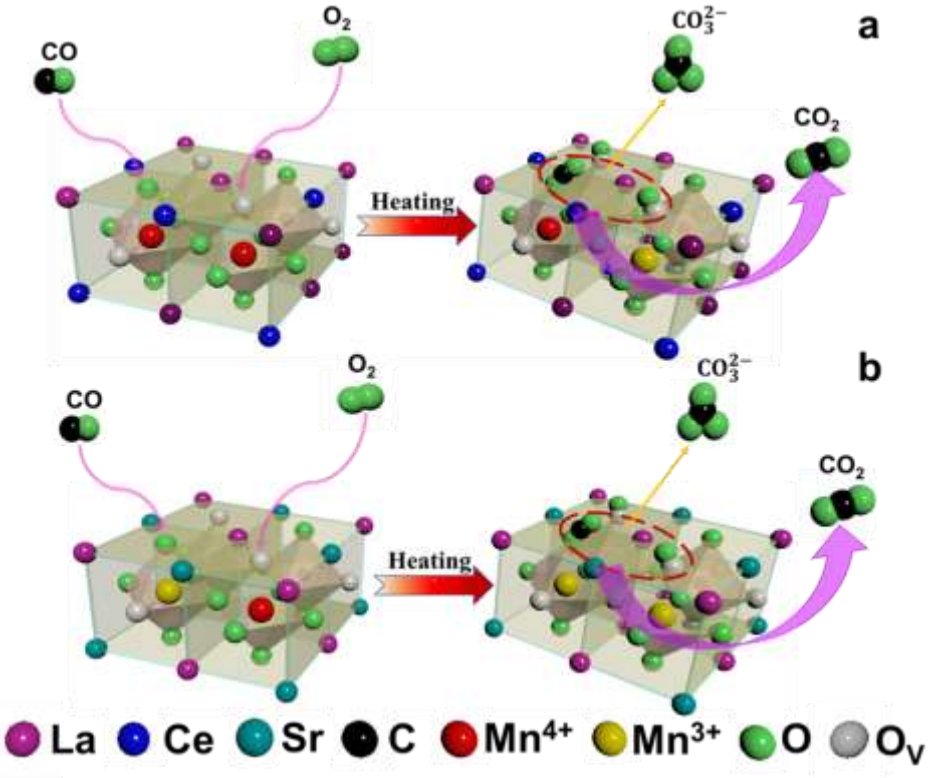

Fig. 12. The reaction pathway of CO self-sustained combustion over the LCMO-SW catalysts (a) and LSMO-SW catalysts (b).

4. Conclusion

CO self-sustained combustion is explored over the $LaMnO_3$ catalyst inserted at A sites by Ce and Sr elements prepared with/without sugar. Catalytic performance for self-sustained CO combustion decline in the order of LCMO-SW> LSMO-SW> LMO-SW> LMO-W> LSMO-W> LCMO-W, corresponding to the T_{50} of 205, 216, 224, 229, 230 and 245 °C, respectively. The Binary search is used to determine quickly the critical equivalence ratio ϕ_C of LCMO-SW as 0.303, 0.272, 0.182, 0.213 and 0.213 within the flow rate of 100–300 ml/min, obtaining the minimum of 0.182 at 200 ml/min. The high-temperature stability test confirms that the LCMO-SW gives 100% CO conversion and that the activities remain almost unchanged after reaction for

12 h, where the temperature of the catalyst bed reaches about 717 °C. The L-H mechanism is suitable for the CO catalytic combustion over the manganese-based perovskite catalysts: the chemisorption of CO and O_2 takes place on manganese sites and oxygen vacancies respectively to produce monodentate carbonates and bicarbonate species, which then decompose to yield CO_2 release. The $LaMnO_3$ inserted by the Ce ions or prepared with sugar is beneficial to promoting the activity, and however, the Sr introduction into A sites inhibits the activity. The LCMO-SW exhibits the highest activity among all the catalysts tested since the Ce introduction and the catalyst prepared with sugar increases Mn^{4+} cations enriched on the catalyst surface and have low-temperature reducibility. Furthermore, the presence of Ce^{3+} in the catalysts advantageous to form vacancies on the catalyst surface facilitates oxygen mobility during CO combustion.

Acknowledgements

We gratefully acknowledge the financial support from the National Natural Science Foundation of China (No. 51776216) and the Strategic Priority Research Program of the Chinese Academy of Sciences (No. XDA21040500).

References

[1] Bin F, Kang R, Wei X, Hao Q, Dou B. Self-sustained combustion of carbon monoxide over $CuCe_{0.75}Zr_{0.25}O_{\delta}$ catalyst: Stability operation and reaction mechanism. Proceedings of the Combustion Institute 2019;37(4):5507–15. https://doi.org/10.1016/j.proci.2018.05.114.

[2] Bin F, Wei X, Li, Bo, Hui KS. Self-sustained combustion of carbon monoxide promoted by the Cu-Ce/ZSM-5 catalyst in $CO/O_2/N_2$ atmosphere. Applied Catalysis B: Environmental 2015;162:282–8. https://doi.org/10.1016/j.apcatb.2014.07.007.

[3] Arens M, Worrell, Ernst, Schleich, Joachim. Energy intensity development of the German iron and steel industry between 1991 and 2007. Energy 2012;45(1):786–

97. https://doi.org/10.1016/j.energy.2012.07.012.
[4] Wu M, Ma, Shiwei, Chen, Shiyi, Xiang, Wenguo. Fe–O terminated $LaFeO_3$ perovskite oxide surface for low temperature toluene oxidation. Journal of Cleaner Production 2020;277:123224. https://doi.org/10.1016/j.jclepro.2020.123224.
[5] Li P, Chen X, Li Y, Schwank JW. Effect of preparation methods on the catalytic activity of $La_{0.9}Sr_{0.1}CoO_3$ perovskite for CO and C_3H_6 oxidation. Catalysis Today 2020. https://doi.org/10.1016/j.cattod.2020.03.012.
[6] Xiao P, Xu X, Zhu J, Zhu Y. In situ generation of perovskite oxides and carbon composites: A facile, effective and generalized route to prepare catalysts with improved performance. Journal of Catalysis 2020;383:88–96. https://doi.org/10.1016/j.jcat.2020.01.007.
[7] Álvarez-Galván MC, La Peña O'Shea VA de, Arzamendi G, Pawelec B, Gandía LM, Fierro J. Methyl ethyl ketone combustion over La-transition metal (Cr, Co, Ni, Mn) perovskites. Applied Catalysis B: Environmental 2009;92(3):445–53. https://doi.org/10.1016/j.apcatb.2009.09.006.
[8] Zhang C, Guo Y, Guo Y, Lu G, Boreave A, Retailleau L et al. $LaMnO_3$ perovskite oxides prepared by different methods for catalytic oxidation of toluene. Applied Catalysis B: Environmental 2014;148-149:490–8. https://doi.org/10.1016/j.apcatb.2013.11.030.
[9] Ponce S, Peña M, Fierro J. Surface properties and catalytic performance in methane combustion of Sr-substituted lanthanum manganites. Applied Catalysis B: Environmental 2000;24(3):193–205. https://doi.org/10.1016/S0926-3373(99)00111-3.
[10] Zhang C, Hua W, Wang C, Guo Y, Guo Y, Lu G et al. The effect of A-site substitution by Sr, Mg and Ce on the catalytic performance of $LaMnO_3$ catalysts for the oxidation of vinyl chloride emission. Applied Catalysis B: Environmental 2013;134-135:310–5. https://doi.org/10.1016/j.apcatb.2013.01.031.
[11] Zhao B, Ran R, Yang L, Wu X, Si Z, Weng D. Comparative study of $La_{1-x}Ce_xMnO^{3+}$delta perovskites and Mn-Ce mixed oxides for NO catalytic oxidation. Journal of Rare Earths 2020;38(8):863–72. https://doi.org/10.1016/j.jre.2020.03.003.
[12] Huang H, Liu Q, Lu B, Wang X, Hu J. LaMnO3-diamond composites as efficient oxygen reduction reaction catalyst for Zn-air battery. Diamond and Related Materials 2019;91:199–206. https://doi.org/10.1016/j.diamond.2018.11.024.
[13] Alifanti M, Kirchnerova J, Delmon B. Effect of substitution by cerium on the activity of $LaMnO_3$ perovskite in methane combustion. Applied Catalysis A: General 2003;245(2):231–44. https://doi.org/10.1016/S0926-860X(02)00644-0.
[14] Xue G, Zhao Y, Liang J, Yuan Y, Wang S, Chen D. Properties of $La_{0.9}Sr_{0.1}MnO_3$ and tourmaline compound catalytic materials for methane combustion. Journal of Rare Earths 2014;32(9):837–41. https://doi.org/10.1016/S1002-0721(14)60150-2.

[15] Gholamrezaei S, Salavati-Niasari M. Sonochemical synthesis of $SrMnO_3$ nanoparticles as an efficient and new catalyst for O_2 evolution from water splitting reaction. Ultrasonics Sonochemistry 2018;40:651–63. https://doi.org/10.1016/j.ultsonch.2017.08.012.
[16] Yan N, Hao Q, Zhao C, Yang D, Dou B, Hui KS et al. Studies on $CuCe_{0.75}Zr_{0.25}O_x$ preparation using bacterial cellulose and its application in toluene complete oxidation. CHEMISTRYSELECT 2019;4(14):4355–63. https://doi.org/10.1002/slct.201900727.
[17] Dudric R, Vladescu A, Rednic V, Neumann M, Deac IG, Tetean R. XPS study on $La_{0.67}Ca_{0.33}Mn_{1-x}Co_xO_3$ compounds. Journal of Molecular Structure 2014;1073:66–70. https://doi.org/10.1016/j.molstruc.2014.04.065.
[18] Tyagi D, Srinivasan S, Wani BN, Bharadwaj SR. XPS Studies of Sr doped La_2CuO_4: A potential cathode material for IT-SOFCs. Materials Today: Proceedings 2018;5(11, Part 2):22950–4. https://doi.org/10.1016/j.matpr.2018.11.022.
[19] Chen H, Li J, Cui W, Fei Z, Tian Q, Liu Q et al. Precise fabrication of surface-reconstructed $LaMnO_3$ perovskite with enhanced catalytic performance in CH_4 oxidation. Applied Surface Science 2020;505:144112. https://doi.org/10.1016/j.apsusc.2019.144112.
[20] Chen J, Shen M, Wang X, Qi G, Wang J, Li W. The influence of nonstoichiometry on $LaMnO_3$ perovskite for catalytic NO oxidation. Applied Catalysis B: Environmental 2013;134-135:251–7. https://doi.org/10.1016/j.apcatb.2013.01.027.
[21] Lima SM, Assaf JM, Peña MA, Fierro J. Structural features of $La_{1-x}Ce_xNiO_3$ mixed oxides and performance for the dry reforming of methane. Applied Catalysis A: General 2006;311:94–104. https://doi.org/10.1016/j.apcata.2006.06.010.
[22] Krishnamoorthy C, Sethupathi K, Sankaranarayanan V. Synthesis of single phase Ce doped nanocrystalline $LaMnO_3$. Materials Letters 2007;61(14):3254–7. https://doi.org/10.1016/j.matlet.2006.11.049.
[23] Khaledian HR, Zolfaghari P, Nezhad PDK, Niaei A, Khorram S, Salari D. Surface Modification of $LaMnO_3$ Perovskite Supported on CeO_2 Using Argon Plasma for High-performance Reduction of NO. Journal of Environmental Chemical Engineering 2020:104581. https://doi.org/10.1016/j.jece.2020.104581.
[24] Li H, Liu F, Helian Y, Yang G, Wu Z, Gao Y et al. Inspection of various precipitant on SrO–based catalyst for transesterification: Catalytic performance, reusability and characterizations. Catalysis Today 2020. https://doi.org/10.1016/j.cattod.2020.06.038.
[25] Huang K, Chu X, Yuan L, Feng W, Wu X, Wang X et al. Engineering the surface of perovskite $La_{0.5}Sr_{0.5}MnO_3$ for catalytic activity of CO oxidation. CHEMICAL COMMUNICATIONS 2014;50(65):9200–3. https://doi.org/10.1039/c4cc00023d.
[26] Cimino S, Lisi L, Rossi S de, Faticanti M, Porta P. Methane combustion and CO

oxidation on $LaAl_{1-x}Mn_xO_3$ perovskite-type oxide solid solutions. Applied Catalysis B: Environmental 2003;43(4):397–406. https://doi.org/10.1016/S0926-3373(03)00023-7.

[27] Ciambelli P, Cimino S, Rossi S de, Faticanti M, Lisi L, Minelli G et al. $AMnO_3$ (A=La, Nd, Sm) and $Sm_{1-x}Sr_xMnO_3$ perovskites as combustion catalysts: structural, redox and catalytic properties. Applied Catalysis B: Environmental 2000;24(3):243–53. https://doi.org/10.1016/S0926-3373(99)00110-1.

[28] Levasseur B, Kaliaguine S. Methanol oxidation on $LaBO_3$ (B=Co, Mn, Fe) perovskite-type catalysts prepared by reactive grinding. Applied Catalysis A: General 2008;343(1):29–38. https://doi.org/10.1016/j.apcata.2008.03.016.

[29] Teng F, Han W, Liang S, Gaugeu B, Zong R, Zhu Y. Catalytic behavior of hydrothermally synthesized $La_{0.5}Sr_{0.5}MnO_3$ single-crystal cubes in the oxidation of CO and CH4. Journal of Catalysis 2007;250(1):1–11. https://doi.org/10.1016/j.jcat.2007.05.007.

[30] Liu Y, Dai H, Du Y, Deng J, Zhang L, Zhao Z et al. Controlled preparation and high catalytic performance of three-dimensionally ordered macroporous $LaMnO_3$ with nanovoid skeletons for the combustion of toluene. Journal of Catalysis 2012;287:149–60. https://doi.org/10.1016/j.jcat.2011.12.015.

[31] Deng J, Dai H, Jiang H, Zhang L, Wang G, He H et al. Hydrothermal Fabrication and Catalytic Properties of $La_{1-x}Sr_xM_{1-y}Fe_yO_3$ (M = Mn, Co) That Are Highly Active for the Removal of Toluene. Environmental Science & Technology 2010;44(7):2618–23. https://doi.org/10.1021/es9031997.

[32] Kang R, Ma P, He J, Li H, Bin F, Wei X et al. Transient behavior and reaction mechanism of CO catalytic ignition over a $CuO–CeO_2$ mixed oxide. Proceedings of the Combustion Institute 2020. https://doi.org/10.1016/j.proci.2020.06.186.

[33] Kaddouri A, Gelin P, Dupont N. Methane catalytic combustion over La–Ce–Mn–O- perovskite prepared using dielectric heating. Catalysis Communications 2009;10(7):1085–9. https://doi.org/10.1016/j.catcom.2008.12.063.

[34] Szabo V, Bassir M, van Neste A, Kaliaguine S. Perovskite-type oxides synthesized by reactive grinding: Part II: Catalytic properties of $LaCo_{(1-x)}Fe_xO_3$ in VOC oxidation. Applied Catalysis B: Environmental 2002;37(2):175–80. https://doi.org/10.1016/S0926-3373(01)00328-9.

[35] Wan Q, Duan L, He K, Li J. Removal of gaseous elemental mercury over a $CeO_2–WO_3/TiO_2$ nanocomposite in simulated coal-fired flue gas. Chemical Engineering Journal 2011;170(2):512–7. https://doi.org/10.1016/j.cej.2010.11.060.

[36] Tsounis C, Wang Y, Arandiyan H, Wong RJ, Toe CY, Amal R et al. Tuning the Selectivity of LaNiO3 Perovskites for CO_2 Hydrogenation through Potassium Substitution. Catalysts 2020;10(4):409. https://doi.org/10.3390/catal10040409.

[37] González Tejuca L, Bell AT, Fierro J, Peña MA. Surface behaviour of reduced $LaCoO_3$ as studied by TPD of CO, CO_2 and H_2 probes and by XPS. Applied Surface Science 1988;31(3):301–16.

https://doi.org/10.1016/0169-4332(88)90095-5.
[38] Cui X, Wang J, Cao J-P, Zhao P-T, Wang Y-X, Yan H et al. Effect of A-site disubstituted of lanthanide perovskite on catalytic activity and reaction kinetics analysis of coal combustion. Fuel 2020;260:116380. https://doi.org/10.1016/j.fuel.2019.116380.
[39] Yi Y, Liu H, Chu B, Qin Z, Dong L, He H et al. Catalytic removal NO by CO over $LaNi_{0.5}M_{0.5}O_3$ (M = Co, Mn, Cu) perovskite oxide catalysts: Tune surface chemical composition to improve N2 selectivity. Chemical Engineering Journal 2019;369:511–21. https://doi.org/10.1016/j.cej.2019.03.066.
[40] Wu Y, Li L, Chu B, Yi Y, Qin Z, Fan M et al. Catalytic reduction of NO by CO over B-site partially substituted $LaM_{0.25}Co_{0.75}O_3$ (M = Cu, Mn, Fe) perovskite oxide catalysts: The correlation between physicochemical properties and catalytic performance. Applied Catalysis A: General 2018;568:43–53. https://doi.org/10.1016/j.apcata.2018.09.022.
[41] Lima SM de, Da Silva AM, Da Costa LO, Assaf JM, Jacobs G, Davis BH et al. Evaluation of the performance of Ni/La_2O_3 catalyst prepared from $LaNiO_3$ perovskite-type oxides for the production of hydrogen through steam reforming and oxidative steam reforming of ethanol. Applied Catalysis A: General 2010;377(1-2):181–90. https://doi.org/10.1016/j.apcata.2010.01.036.
[42] Urán L, Gallego J, Ruiz W, Bailón-García E, Bueno-López A, Santamaría A. Monitoring intermediate species formation by DRIFT during the simultaneous removal of soot and NOx over $LaAgMnO_3$ catalyst. Applied Catalysis A: General 2019;588:117280. https://doi.org/10.1016/j.apcata.2019.117280.
[43] Kang R, Wei X, Ma P, Bin F, He J, Hao Q et al. Self-sustained combustion of CO with transient changes and reaction mechanism over $CuCe_{0.75}Zr_{0.25}O_\delta$ powder for honeycomb ceramic catalyst. Fuel 2020;263:116637. https://doi.org/10.1016/j.fuel.2019.116637.
[44] Wu Y, Liu H, Li G, Jin L, Li X, Ou X et al. Tuning composition on B sites of $LaM_{0.5}Mn_{0.5}O_3$ (M = Cu, Co, Fe, Ni, Cr) perovskite catalysts in NOx efficient reduction. Applied Surface Science 2020;508:145158. https://doi.org/10.1016/j.apsusc.2019.145158.
[45] Biesinger MC, Payne BP, Grosvenor AP, Lau LW, Gerson AR, Smart RS. Resolving surface chemical states in XPS analysis of first row transition metals, oxides and hydroxides: Cr, Mn, Fe, Co and Ni. Applied Surface Science 2011;257(7):2717–30. https://doi.org/10.1016/j.apsusc.2010.10.051.
[46] Zhang C, Wang C, Zhan W, Guo Y, Guo Y, Lu G et al. Catalytic oxidation of vinyl chloride emission over $LaMnO_3$ and $LaB_{0.2}Mn_{0.8}O_3$ (B=Co, Ni, Fe) catalysts. Applied Catalysis B: Environmental 2013;129:509–16. https://doi.org/10.1016/j.apcatb.2012.09.056.
[47] Tejuca LG, Bell AT, Fierro JLG, Tascón JMD. Temperature-programmed desorption study of the interactions of H_2, CO and CO_2 with $LaMnO_3$. Journal of the Chemical Society, Faraday Transactions 1: Physical Chemistry in Condensed

Phases 1987;83(10):3149–59.
[48] Corberán VC, Tejuca LG, Bell AT. Surface reactivity of reduced $LaFeO_3$ as studied by TPD and IR spectroscopies of CO, CO_2 and H_2. Journal of Materials Science 1989;24(12):4437–42. https://doi.org/10.1007/BF00544527.